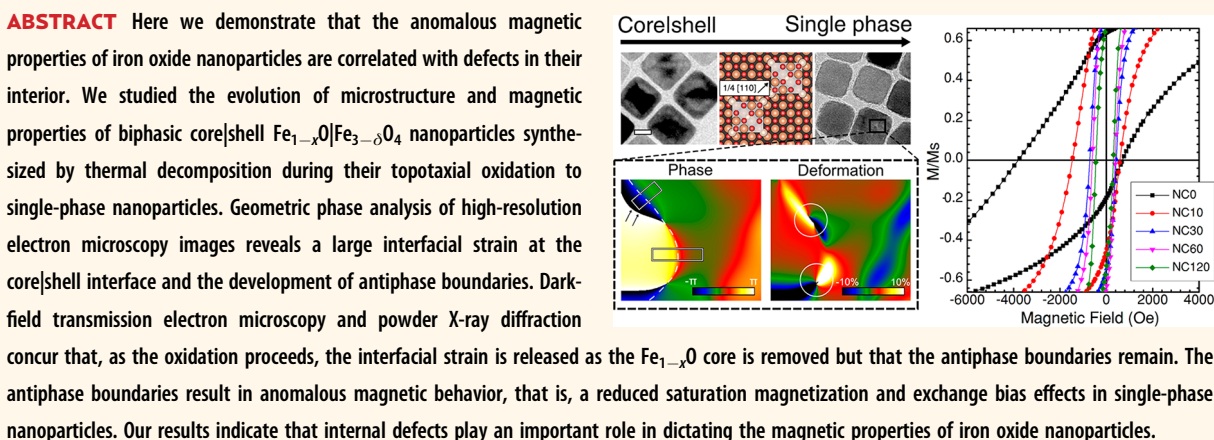


Anomalous Magnetic Properties of Nanoparticles Arising from Defect Structures: Topotaxial Oxidation of $\text{Fe}_{1-x}\text{O}|\text{Fe}_{3-\delta}\text{O}_4$ Core|Shell Nanocubes to Single-Phase Particles

Erik Wetterskog, Cheuk-Wai Tai, Jekabs Grins, Lennart Bergström, and German Salazar-Alvarez*

Department of Materials and Environmental Chemistry, Arrhenius Laboratory, Stockholm University, SE-106 91 Stockholm, Sweden



KEYWORDS: iron oxide · core|shell · nanoparticles · defects · antiphase boundary · electron microscopy · exchange bias

Iron oxide nanoparticles (IONPs) are currently being actively researched for a range of technological applications, ranging from contrast agents for MRI, hyperthermia, sensing and targeted drug delivery to energy storage.^{1–3} Monodispersed IONPs, typically synthesized in organic media, are also interesting model systems for studying magnetism at the nanoscale both as isolated nanoparticles and in ordered arrays.^{4–6} Much efforts have recently been devoted to the synthesis of multicomponent nanoparticles (e.g., core|shell, Janus particles) with the aim of improving and tuning their properties.^{7–10} The thermal decomposition of metal oleates is a very versatile and extensively used route for the synthesis of monodispersed nanoparticles with well-defined compositions.¹⁰ Thermal decomposition of iron-oleate-based precursors produces IONPs with compositions that vary with the synthesis temperature and the reaction atmosphere, but also with

other factors such as availability of unsaturated bonds in the synthesis solvent.^{11,12} It has been shown that the thermal decomposition process generates CO, which participates in the reduction of iron(III) and can thus result in the formation of Fe and Fe_{1-x}O nanoparticles.^{11–14} Thus, the IONPs produced by thermal decomposition of iron oleate may have a complex composition consisting of iron oxide phases with very different magnetic properties. Indeed, previous work has identified IONPs that can be composed of $\text{Fe}_{3-\delta}\text{O}_4$, for example, which is a solid solution of the end members Fe_3O_4 and $\gamma\text{-Fe}_2\text{O}_3$ (both ferrimagnets, FiM); Fe_{1-x}O (wüstite) an antiferromagnet, AFM; or Fe, a ferromagnet, FM.^{15–17} The thermodynamic landscape of the iron oxides is strongly influenced by surface effects and therefore subject to size-driven crossovers of the Gibbs free energies. This results in a higher stability for $\gamma\text{-Fe}_2\text{O}_3$ relative to $\alpha\text{-Fe}_2\text{O}_3$ for small particle sizes

* Address correspondence to german@mmk.su.se.

Received for review May 16, 2013 and accepted July 30, 2013.

Published online July 30, 2013
10.1021/nn402487q

© 2013 American Chemical Society

(≈ 15 nm) and anhydrous conditions.¹⁸ Exploiting the formation of Fe_{1-x}O and its subsequent oxidation in air has enabled the study of the exchange coupling of core|shell $\text{Fe}_{1-x}\text{O}|\text{MFe}_2\text{O}_4$ nanoparticles with other isostructural ferrimagnetic (FiM) oxides (e.g., CoFe_2O_4 , Fe_3O_4 , $\gamma\text{-Fe}_2\text{O}_3$).^{19–21} Although the chemical transformations of Fe_{1-x}O , $\text{Fe}_{1-x}\text{O}|\text{Fe}_{3-\delta}\text{O}_4$, and $\text{Fe}_{3-\delta}\text{O}_4$ nanoparticles have been investigated to some extent,^{13,14,17,22–25} their anomalous magnetic properties, such as reduced saturation magnetization compared to bulk values,^{15,26–30} exchange bias in seemingly single-phase nanoparticles,^{5,27,28,31–34} and high-field susceptibilities,^{27,28,33,34} are still poorly understood and commonly ascribed to spin canting or defects at the particles' outer surface.^{35–40} However, while surface effects could indeed be important in smaller nanoparticles, their significance is expected to diminish drastically with increasing particle size. Recently, we showed in a study performed using polarized small-angle neutron scattering (SANS) that, although the nanoparticles are associated with a canted surface layer of subnanometer thickness, the magnetic moment of the particle interior is also significantly reduced relative to the bulk phase.²⁶ This highlights that studies linking the structural features (e.g., defects) in the interior of IONPs to the observed anomalous magnetic properties are clearly needed. In fact, reports investigating the correlation between the particles' internal structure and their magnetic properties are very scarce: Luigjes and co-workers showed that the presence of dislocations and twin boundaries in IONPs results in large discrepancies between the magnetic and geometric size distributions,⁴¹ whereas Levy and co-workers noted that magnetic disorder in their IONPs was caused by highly strained regions in the particle interior.³³ Despite these recent efforts, the chemical origin of these defects has remained elusive.

In this work, we have studied the structural and magnetic evolution of biphasic core|shell $\text{Fe}_{1-x}\text{O}|\text{Fe}_{3-\delta}\text{O}_4$ nanoparticles to single-phase $\text{Fe}_{3-\delta}\text{O}_4$ particles during a controlled oxidation procedure. The oxidation preserves the particles' cubic shape and size of about 20 nm, allowing a direct comparison of the exchange-coupling phenomena based on compositional and microstructural differences only. Geometric phase analysis (GPA) of high-resolution electron microscopy (HRTEM) images reveals a large interfacial strain at the core|shell interface and the presence of antiphase boundaries (APBs). Dark-field transmission electron microscopy (DFTEM) and powder X-ray diffraction (PXRD) concur that, as the oxidation proceeds, the interfacial strain is released as the Fe_{1-x}O core is removed but the antiphase boundaries remain. The perseverance of the antiphase boundaries in the fully oxidized single-phase IONPs results in anomalous magnetic behavior, that is, a reduced saturation magnetization and emergence of exchange-coupling effects. Our results demonstrate that misfit dislocations (resulting from interfacial strains) and APBs are characteristic internal defects in the core|shell particles, whereas after removal of the

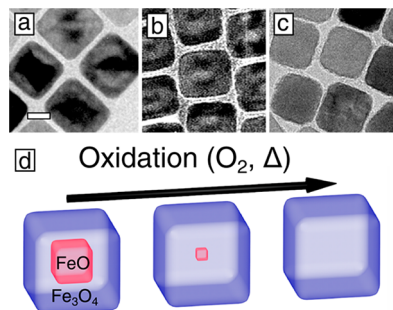


Figure 1. TEM images and schematic illustration of iron oxide nanocubes at different degrees of oxidation. Bright-field TEM micrographs of (a) as-synthesized nanocubes (NC0) with an obvious $\text{Fe}_{1-x}\text{O}|\text{Fe}_{3-\delta}\text{O}_4$ core|shell structure; (b) nanocubes after 30 min of oxidation where the core|shell structure is fading (NC30); and (c) nanocubes after 120 min of oxidation (NC120) with a single-phase structure (scale bar: 10 nm). (d) Illustration of the gradual elimination of the core of the $\text{Fe}_{1-x}\text{O}|\text{Fe}_{3-\delta}\text{O}_4$ particles during the gentle oxidation procedure.

core, APBs are the prevailing internal defects in IONPs prepared by thermal decomposition methods. These results pave the way to obtain size- and shape-controlled nanoparticles with magnetic properties close to the theoretical values.

RESULTS AND DISCUSSION

Monodisperse nanocubes were synthesized by decomposition of iron(III) oleate at 350 °C under an argon atmosphere. As can be seen in Figure 1a, the synthesis procedure that involves several washing steps in ambient atmosphere^{14,21} produces core|shell nanocubes. TEM analysis of the images shows that the nanocubes are monodisperse with an average edge length of $l_{\text{NC}0} = 23.2 \pm 2.6$ nm (see the Experimental Section for a description of the samples and Supporting Information Figure S5 for the size determination). The contrast in the bright-field TEM (BFTEM) images originates from the occurrence of two phases, that is, a Fe_{1-x}O core and $\text{Fe}_{3-\delta}\text{O}_4$ shell with a thickness of ≈ 5 nm (see Figure 1a). The core|shell $\text{Fe}_{1-x}\text{O}|\text{Fe}_{3-\delta}\text{O}_4$ particles were then subjected to a controlled oxidation procedure, by bubbling air through a hot (150 °C) nanocube dispersion. Aliquots were drawn at different times to produce six additional nanocube samples with different degrees of oxidation, and these will be referred to as NC t , where t (min) indicates the oxidation time. The process does not modify the shape of the nanocubes nor the size beyond the expected (*i.e.*, $l_{\text{NC}120} = 23.4 \pm 1.8$ nm). Figure 1b,c shows that the core size is significantly reduced after 30 min (NC30) and finally eliminated after 120 min of oxidation (NC120). Using PXRD and the Rietveld method, we determined the phase composition and lattice parameters of the samples that were retrieved after various oxidation times (NC0–NC240; see the PXRD patterns in Figure S2). The as-synthesized and briefly oxidized nanocubes, NC0 and NC10, display Fe_{1-x}O fractions of

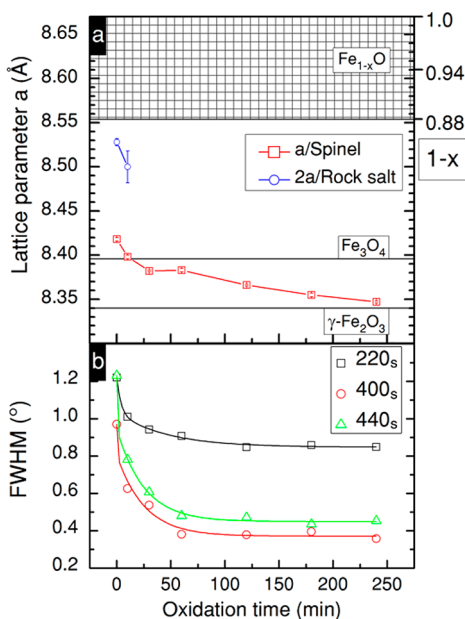


Figure 2. Variation of lattice parameter and diffraction line width for nanocubes as a function of oxidation time. (a) Spinel and doubled rock salt lattice parameters as determined by Rietveld refinement. Solid lines indicate the literature values for bulk Fe_3O_4 and $\gamma\text{-Fe}_2\text{O}_3$.⁴⁸ The hashed area indicates the range of lattice parameters of Fe_{1-x}O as it varies with the composition displayed at the right axis.⁴² (b) Full width at half-maximum (fwhm) of the 220_s , 400_s , and 440_s diffraction lines, corresponding to the spinel structure as obtained by line profile fits. For NC10 and NC30, overlapping lines from Fe_{1-x}O were included in the fitting. The curves are a guide to the eye.

$y_{\text{FeO,NC}0} = 0.09 \pm 0.01$ and $y_{\text{FeO,NC}10} = 0.03 \pm 0.01$ (by weight). Assuming a cube-shaped wüstite (Fe_{1-x}O) core, y_{FeO} can be used to estimate the core size, that is, $I_c = (l_p^3 y_{\text{FeO}})^{1/3}$, where l_p and l_c are the size of the particle and its core. This results in average edge lengths of the Fe_{1-x}O cores of $I_c \approx 10.0 \pm 0.5$ and 7.0 ± 1.0 nm for NC0 and NC10, respectively. When the nanocubes have been subjected to an oxidation time of 30 min or more and the relative size of the Fe_{1-x}O core is reduced to a few nanometers, it is not possible to quantitatively determine the phase composition from the PXRD. Figure 2a shows that the lattice parameter of Fe_{1-x}O in the NC0 nanocubes is substantially smaller than those within the compositional limit of Fe_{1-x}O ($1-x = 0.88-0.96$).⁴² The smaller lattice parameter corresponds to a 0.3–0.9% lattice compression compared to unconfined bulk Fe_{1-x}O ($1-x = 0.88-0.96$), and the Fe_{1-x}O core is further compressed during the initial stage of oxidation with the NC10 displaying a compression of 0.6–1.5%. Indeed, a similar lattice contraction with decreasing size of the wüstite phase has been previously reported by a number of groups studying the synthesis of Fe_{1-x}O and $\text{Fe}_{1-x}\text{O}|\text{Fe}_{3-\delta}\text{O}_4$ nanoparticles.^{14,17,24} Vegard's law⁴² has been used to estimate the composition of some of these particles, resulting in Fe_{1-x}O ($1-x \approx 0.8$) with a composition well below the reported stability range ($1-x = 0.88-0.96$) and very close to

Fe_3O_4 (i.e., $\text{Fe}_{0.75}\text{O}$).^{17,24} However, Vegard's law may not be valid in confined systems (e.g., core|shell configurations) where interfacial effects dominate.^{43–46} Instead, the smaller value of the lattice parameter of the Fe_{1-x}O core (see Figure 2, NC0–NC10) suggests that the Fe_{1-x}O core is heavily compressed as a result of the relatively large lattice mismatch of $\approx 1.3\%$ between the core and the shell, as determined experimentally (≈ 1.9 – 2.5% in the case of the bulk phases). Comparing the reduced unit cell volume ($V/V_0 \approx 0.99$ – 0.97 for compositions $1-x = 0.88$ – 0.96) with compressibility measurements,⁴⁷ the PXRD results suggest that the contracted Fe_{1-x}O lattice parameter of NC0 correlates to a pressure exerted on the core corresponding to ≈ 1 – 5 GPa. Figure 2a also shows that the $\text{Fe}_{3-\delta}\text{O}_4$ lattice of NC0 is slightly expanded ($\approx 0.3\%$) compared to its commonly accepted bulk value (8.396 Å).⁴⁸ During the early stage of oxidation (i.e., NC10), the lattice parameter of the $\text{Fe}_{3-\delta}\text{O}_4$ shell relaxes to the bulk value for Fe_3O_4 which is followed by a gradual decrease toward a value close to that of $\gamma\text{-Fe}_2\text{O}_3$ (8.340 Å).⁴⁸

The unit cell expansion of the $\text{Fe}_{3-\delta}\text{O}_4$ in NC0 (i.e., $V/V_0 \approx 1.01$) is comparable to the Fe_{1-x}O unit cell contraction, $V/V_0 \approx 0.99$ – 0.97 , but becomes negligible as the thickness of the $\text{Fe}_{3-\delta}\text{O}_4$ shell increases (i.e., for NC10), as could be expected for a solid–solid interfaces in nanoparticles which adapt mutually in order to facilitate epitaxial or topotaxial growth.⁴⁹

Figure 2b shows how the full width at half-maximum (fwhm) of the 220_s , 400_s , and 440_s lines varies with oxidation time. The 220_s diffraction line is associated with the cations ordered in tetrahedral interstitials, characteristic of the spinel structure, whereas the lines 400_s and 440_s of the spinel structure overlap with the 200_{RS} and 220_{RS} lines of the rock salt (RS) structure. These diffraction lines are subject to anisotropic line broadening, as a result of the chemical process: the octahedral face-centered cubic (fcc) O^{2-} sublattice and the majority of octahedral $\text{Fe}^{II}/\text{Fe}^{III}$ positions are identical both in Fe_{1-x}O and $\text{Fe}_{3-\delta}\text{O}_4$ and generate the 400_s and 440_s diffraction lines of the spinel structure. Conversely, the formation of a long-range-ordered tetrahedral Fe^{III} sublattice (which can be seen as equivalent to the nucleation of $\text{Fe}_{3-\delta}\text{O}_4$) generates, amongst others, the 111_s and 220_s lines in $\text{Fe}_{3-\delta}\text{O}_4$ for which the Fe_{1-x}O phase has no counterparts. Figure 2b shows that all these three diffraction lines narrow down as oxidation proceeds, with the 400_s and the 440_s lines being significantly more influenced by oxidation than the 220_s line. This anisotropic line broadening could be due to anisotropic size broadening (e.g., changes in the crystallite shape) and/or anisotropic strain broadening (e.g., unequal densities of defects along different crystallographic directions).⁵⁰ The nanoparticle shape was accounted for by introducing calculated anisotropic constants, k_{hkl} ($k_{200} = 0.862$ and $k_{220} = 0.789$ for a cubic particle in a cubic crystal system) in the well-known

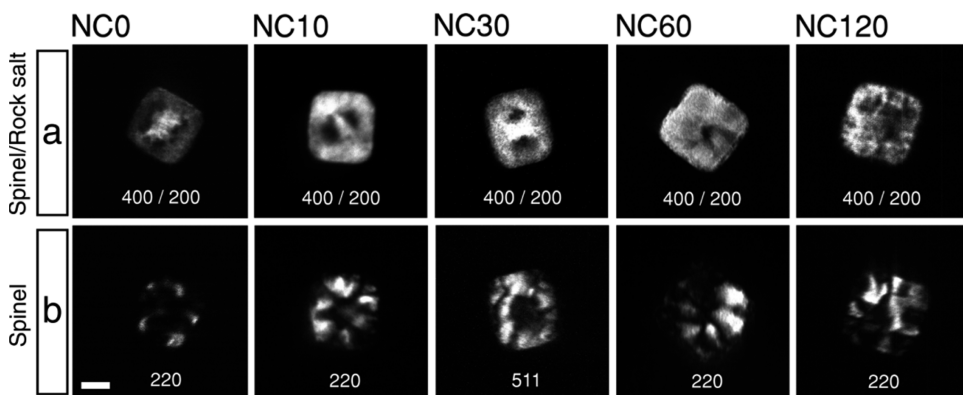


Figure 3. Dark-field transmission electron microscopy (DFTEM) images of iron oxide nanocubes at different degrees of oxidation; NC0–NC120. The DFTEM images were formed using the diffracted beams indicated in each image. (a) Images formed by overlapping reflections of Fe_{1-x}O and the $\text{Fe}_{3-\delta}\text{O}_4$, $400_{\text{S}}/200_{\text{RS}}$. (b) Images formed exclusively from $\text{Fe}_{3-\delta}\text{O}_4$ reflections (scale bar: 10 nm; all images have the same magnification).

Scherrer equation. This yields $d_{\text{eff}} = (k_{hk\bar{l}}\lambda)/(2\omega \cos \theta)$, the effective size of crystal along the normal of the diffraction plane where λ is the wavelength, 2ω is the fwhm of the diffraction peak (in radians), and θ is the Bragg angle.⁵¹ The fwhm of the 220_{S} and 400_{S} diffraction lines for NC0 and N120 translates into effective crystal sizes $d_{400_{\text{S}}} \approx 8$ nm and $d_{220_{\text{S}}} \approx 6.5$ nm and $d_{400_{\text{S}}} \approx 20$ nm and $d_{220_{\text{S}}} \approx 9$ nm for the core|shell nanocubes NC0 and the single-phase nanocubes NC120, respectively (see Supporting Information). Interestingly, for the core|shell nanocubes NC0, $d_{400_{\text{S}}}$ is considerably smaller than the primary crystallite size determined by TEM ($l_{\text{NC}0}$), likely due to the strain between the newly generated $\text{Fe}_{3-\delta}\text{O}_4$ subdomains (or nuclei) on the Fe_{1-x}O lattice. In case of the single-phase nanocubes NC120, $d_{400_{\text{S}}}$ is in reasonable agreement with the edge length ($l_{\text{NC}120}$) of nanocubes obtained from TEM. However, the coherence length corresponding to the spinel-only diffraction line $d_{220_{\text{S}}}$ is considerably smaller than $d_{400_{\text{S}}}$ in all cases. The divergence of the trends of the 220_{S} and 400_{S} (and also 440_{S}) diffraction line widths indicates a significant discrepancy between the long-range order of the tetrahedral and the octahedral sublattices in the spinel structure as it develops during the oxidation of the nanocubes. Moreover, this discrepancy persists over long oxidation times, as the fwhm of the 220_{S} line does not narrow further beyond 120 min.

The discrepancy between the particle sizes observed by BFTEM and PXRD was further investigated in real space by means of dark-field TEM (DFTEM), where we could selectively image either both the spinel ($\text{Fe}_{3-\delta}\text{O}_4$) and rock salt (Fe_{1-x}O) structures or only the (growing) spinel subdomains. DFTEM is highly sensitive to local changes in the crystallographic orientation of the specimen and is therefore effective for imaging defects and domain structures in nanostructured materials. Figure 3 shows DFTEM images of NC0–NC120 that were acquired by using diffracted beams corresponding to either some overlapping spinel (S) and rock salt reflections (RS) (i.e., $\mathbf{g}_{400_{\text{S}}}/\mathbf{g}_{200_{\text{RS}}}$, Figure 3a)

or exclusively from the spinel reflections (i.e., $\mathbf{g}_{220_{\text{S}}}$ or $\mathbf{g}_{511_{\text{S}}}$, Figure 3b). The combined rock salt/spinel DFTEM images (Figure 3a) show that the nanocubes change from a clear core|shell motif (NC0, NC10, and NC30) toward a single-phase appearance; that is, the contrast becomes progressively more homogeneous (NC60, NC120). The oxidation of Fe_{1-x}O to $\text{Fe}_{3-\delta}\text{O}_4$ (observed as a removal of the core|shell motif) is in agreement with the convergence of the size of the octahedral sublattice (as observed by PXRD) to that of a single crystal (as observed by TEM), that is, $d_{400} \rightarrow l_{\text{NC}120}$. Conversely, the growth of the $\text{Fe}_{3-\delta}\text{O}_4$ phase is illustrated by the evolution of the spinel-only DFTEM images (Figure 3b). For the NC0 core|shell cubes, alternating bright and dark areas indicate that there are multiple nucleation points of the $\text{Fe}_{3-\delta}\text{O}_4$ on the $(\text{Fe}_{1-x}\text{O})$ cube surface, as suggested by the spatial separation of these subdomains. These subdomains have a size around ≈ 5 nm, based on estimates using the faint images resulting from the weak intensity of the $\mathbf{g}_{220_{\text{S}}}$ beam. As the oxidation progresses (i.e., NC10, NC30), the $\text{Fe}_{3-\delta}\text{O}_4$ subdomains spread at the surface (and inward) to a point where they meet and develop boundaries. First after 60 min of oxidation (i.e., NC60) does the spinel subdomain structure extend throughout the volume of the cube, with subdomains oriented radially outward from the center. Upon prolonged oxidation (NC120), the subdomain structure develops further into a mosaic-like texture separated by sharp boundaries (see also Figure S7, Supporting Information, for a DFTEM image of an ensemble of NC120 nanocubes). At this point, vacancy ordering in the spinel structure occurs (as observed through the appearance of weak superstructure reflections; see Figure S11), indicating the formation of $\gamma\text{-Fe}_2\text{O}_3$ and also the (complete) depletion of Fe^{II} .

Interestingly, the core|shell motif persists after 30 min of gentle oxidation (NC30) and is clearly seen both in the combined rock salt/spinel and the spinel-only image. In fact, a core|shell motif can be observed in

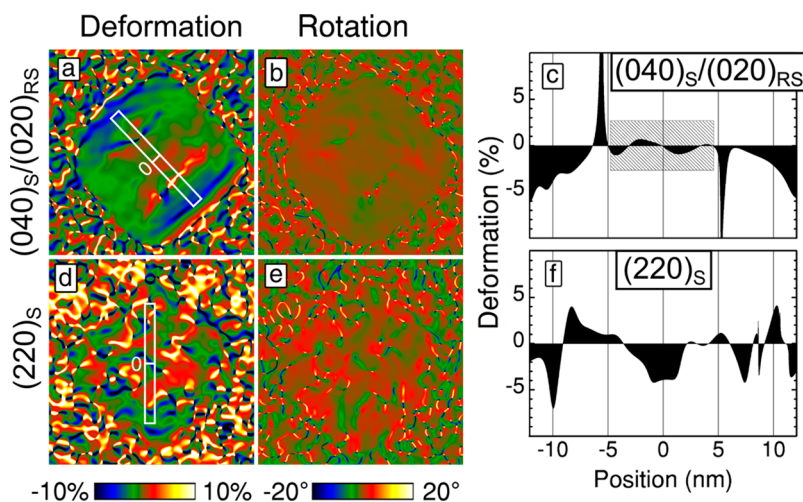


Figure 4. Lattice deformation and rotation maps of a core|shell NCO nanocube. (a,d) Lattice deformation and (b,e) lattice rotation maps obtained by GPA of the $(040)_S/(020)_{RS}$ and the $(220)_S$ reflections oriented parallel to the white rectangle. (c,f) Lattice deformation profiles obtained by integration from the bottom to the top of the white rectangles.

BFTEM images for all NC30 nanocubes that are aligned close to a $\langle 100 \rangle$ zone axis (see Figure 1b and Supporting Information Figure S9). The core size appears to constitute a large fraction of the nanocube core volume, which is surprising given that the fraction of Fe_{1-x}O in the NC30 nanocubes is so small that it is effectively undetected by PXRD. The origin of the core|shell structure in NC30 is therefore not chemical contrast but merely indicates the presence of defects, such as strain field and/or misorientation of subdomains. This suggests that the common approach of determining the Fe_{1-x}O content directly from BF or DFTEM images, by directly measuring the perceived Fe_{1-x}O core sizes, is likely to produce inaccurate results. Note that the observed intensity variations in the spinel-only images are not a consequence of polycrystalline texture, as the electron diffraction patterns in each case are spot patterns characteristic of a single crystal (see Figure S6, Supporting Information).

The distribution and evolution of the subdomain structures (and their interfaces with the rock salt host lattice) were further studied with geometric phase analysis (GPA), by comparing the internal structure of a core|shell nanocube (NC0) to that of an oxidized single-phase nanocube (NC120). GPA enables the determination of crystal lattice deformations directly from high-resolution TEM images and has been applied to a number of different nanostructured systems, such as semiconductor nanowires and epitaxial heterostructures.^{52–56} During GPA, a phase image is first generated from a Fourier filtered power spectrum of the image. The geometric phase shift of the lattice fringe is then used to generate maps of the deformation and rotation of the lattice fringes, relative to a reference area (see Supporting Information for details). The GPA method operates on either an individual Fourier component or a pair of noncollinear Fourier components producing a fringe deformation map or a

strain map, respectively.⁵⁵ In analogy with the DFTEM procedure, it is possible to analyze the deformation of the $(040)_S/(020)_{RS}$ and $(220)_S$ lattice fringe images independently (*i.e.*, the lattice fringe images assigned to the combined spinel/rock salt components and spinel-only component, respectively).

Starting with the core|shell nanocube (NC0, Figure 4), we note that the deformation of the $(040)_S/(020)_{RS}$ lattice fringes (Figure 4a,c) is rather uniform ($\pm 1\%$) in the center of the nanocube (see dashed area in Figure 4c), indicating a relatively homogeneous lattice strain in the Fe_{1-x}O core. Note that the magnitude of the lattice deformation changes abruptly ($>10\%$) at a distance of ≈ 5 nm perpendicular from the nanocube center. The discontinuities in the lattice deformation map along this line can be ascribed to misfit dislocations (see Figure S12), concentrated around the $\text{Fe}_{1-x}\text{O}|\text{Fe}_{3-\delta}\text{O}_4$ interface, similar to those observed in multimetallic core|shell nanoparticles.⁵⁷ Between the core/shell interface and the cube's outer surface, there is a gradual compression of the lattice relative to the Fe_{1-x}O core, corresponding to the shorter lattice parameter of the $\text{Fe}_{3-\delta}\text{O}_4$ spinel shell. The magnitude of the $(040)_S/(020)_{RS}$ lattice contraction in the $\text{Fe}_{3-\delta}\text{O}_4$ shell varies from ≈ 0 – 6% relative to the Fe_{1-x}O core, increasing toward the particle's outer surface. This deformation gradient can in part be ascribed to surface relaxation of the spinel structure (at the nanoparticle's outer surface) but could also indicate that there is a compositional gradient in the $\text{Fe}_{3-\delta}\text{O}_4$ shell. Note that the $(040)_S/(020)_{RS}$ lattice rotation map (Figure 4b) is essentially free from features, and that the average rotational disorder is low except at the $\text{Fe}_{1-x}\text{O}|\text{Fe}_{3-\delta}\text{O}_4$ interface, where it is substantial due to the presence of misfit dislocations. The low rotational disorder in the $(040)_S/(020)_{RS}$ lattice fringe image is likely the result of the topotaxial oxidation of Fe_{1-x}O to $\text{Fe}_{3-\delta}\text{O}_4$ which preserves the

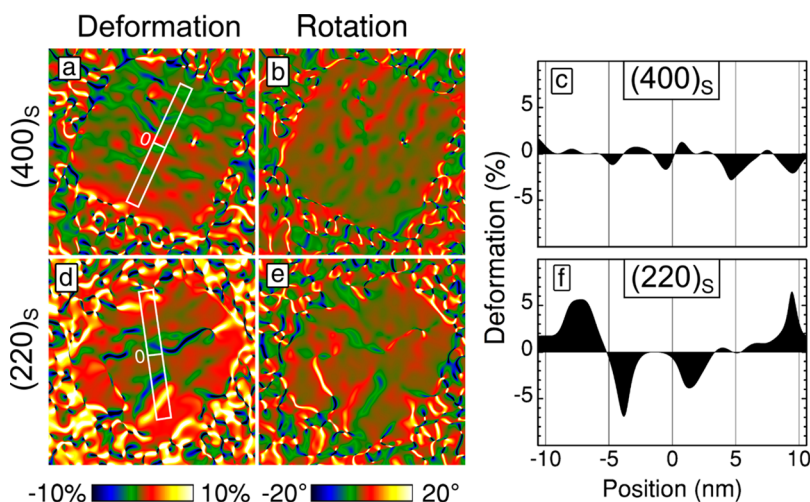


Figure 5. Lattice deformation and rotation maps of a single-phase NC120 nanocube. (a,d) Lattice deformation and (b,e) lattice rotation maps obtained by GPA of the $(400)_S$ and the $(220)_S$ reflections oriented parallel to the white rectangle. (c,f) Lattice deformation profiles obtained by integration from the bottom to the top of the white rectangles.

rotational order of the oxygen fcc sublattice. Conversely, the magnitude of the $(220)_S$ lattice deformation (Figure 4d,f) varies substantially ($\pm 5\%$) within the nanocube and appears to be correlated to the formation of $\text{Fe}_{3-\delta}\text{O}_4$ subdomains, which were also observed in the DFTEM images (Figure 3). Multiple regions of large deformation give rise to a number of discontinuities that appear simultaneously in both the deformation and the rotation map (Figure 4e). Note that this texture appears to be uncorrelated to the core|shell texture observed in the $(040)_S/(020)_{RS}$ images. The growth of the $\text{Fe}_{3-\delta}\text{O}_4$ phase from the particle surface and inward can be understood by considering the oxidation mechanism of the core|shell particles. As Fe_{1-x}O is not oxygen-deficient,⁵⁸ the number of oxygen vacancies is small, limiting the oxygen diffusion through the wüstite lattice. The oxygen adsorbs onto the outer surface of the nanocubes, and the resulting oxygen potential gradient promotes the diffusion of iron(II) from the iron(II)-rich Fe_{1-x}O core to the outer surface of the particle, leaving cation vacancies behind.⁵⁹ Note that the cation diffusion outward from the particle core will cause the composition of Fe_{1-x}O to change, which could be the origin of the small difference in the lattice parameter of Fe_{1-x}O between NC0 and NC10.

The corresponding rotation and deformation maps for an oxidized single-phase nanocube (NC120) are shown in Figure 5 (additional particles are shown in the Supporting Information, Figure S13). The $(400)_S$ lattice deformation map (Figure 5a) has evolved to a uniform texture, and the differences between the lattice parameter of the core and the shell have vanished. The magnitude of deformation of the $(400)_S$ lattice fringes (see Figure 5c) is also considerably smaller ($\pm 1\text{--}2\%$) than that of the core|shell nanocube (NC0). The rotational disorder in $(400)_S$ is also low (Figure 5b) and comparable to that of NC0. Apart from the

inclusion of a few trapped defects, the misfit dislocations originally present at the $\text{Fe}_{1-x}\text{O}|\text{Fe}_{3-\delta}\text{O}_4$ interface are removed during the topotaxial oxidation. In contrast to this, although the lateral size of the spinel subdomains appears to have coarsened, the deformation of the $(220)_S$ sublattice is still significant (Figure 5d,f) and its magnitude is similar to that of the core|shell NC0 ($\pm 5\%$).

The features observed in the $(220)_S$ lattice fringe deformation maps of NC0 and NC120 (Figure 4d, Figure 5d, as well as in the fwhm of the diffraction line in Figure 2b) can be understood from the crystal structure of the phases involved. Fe_{1-x}O is a nonstoichiometric oxide with a defective rock salt structure based on a cubic close-packed oxygen sublattice where each cation vacancy \diamond is compensated by two trivalent iron ions (i.e., $\text{Fe}^{II}_{1-3x}\text{Fe}^{III}_{2x}\diamond\text{O}$). These trivalent ions can diffuse and occupy both tetrahedral and octahedral interstices in the oxygen fcc sublattice⁵⁸ where, for each oxide ion, there is one octahedral site occupied by ferrous ions and two empty tetrahedral sites. Alternatively, the spinel structure consists of a similar cubic close-packing of oxide ions where trivalent and divalent ions occupy only half of the octahedral places and one-quarter of the tetrahedral voids. This results in eight different possible ways that the spinel lattice can grow on a rock salt structure.^{60–62} These nuclei, or subdomains, can be rotated by 90° with respect to each other, shifted by $1/4 [110]$ (as seen in Figure 6f), $1/2 [100]$, or by a combination of two shifts or a shift and a rotation. In this way, the coalescence of two Fe_3O_4 subdomains of different types results in the formation of an antiphase boundary (APB). Once formed, these defects cannot be removed without a significant diffusion of cations.⁶² The formation of APBs in the $\text{Fe}_{3-\delta}\text{O}_4$ shell can probably be generalized to all synthesis methods where a spinel phase (e.g., MFe_2O_4

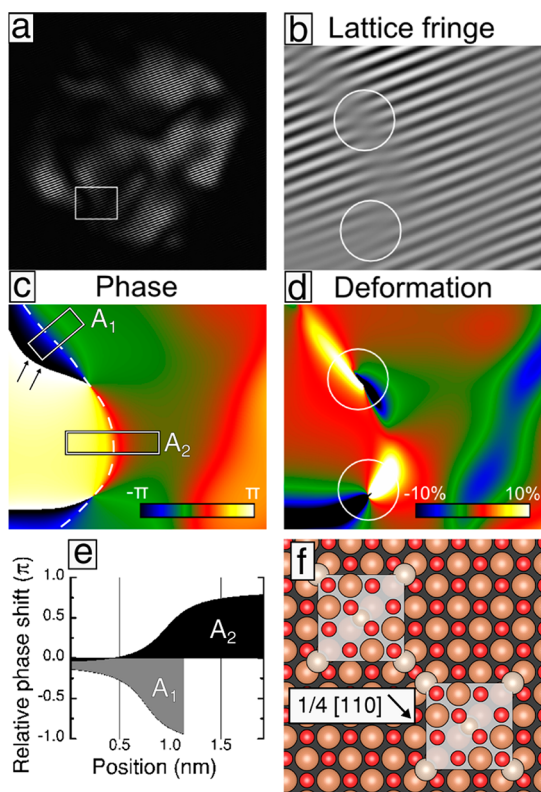


Figure 6. Antiphase boundaries in a NC120 single-phase nanocube. (a) Fourier filtered image obtained by using the 220_S reflection. (b) Lattice fringe image from the area highlighted in (a). (c) Phase and (d) deformation map of the lattice fringe image. Two dislocations are highlighted by white circles in the lattice fringe image and the deformation map. The APB is highlighted by the dashed white line in the phase map. (e) Integrated relative phase shift from the two rectangular areas (A_1 , A_2) in the phase map. (f) Schematic sketch of two Fe_3O_4 unit cells that have nucleated on an idealized FeO surface, related to each other by an antiphase shift.

($M = \text{Fe}, \text{Co}, \text{Mn}$), Co_3O_4 , Mn_3O_4) nucleates on a rock salt structure (e.g., Fe_{1-x}O , Mn_{1-x}O , and Co_{1-x}O) or a structure with an fcc oxygen sublattice. Indeed, APBs have been extensively studied in thin epitaxial Fe_3O_4 films grown on MgO surfaces, a system where the phases exhibit identical symmetry relations as those in the present study.^{60,62–69}

A quantitative assessment of all the different types of APBs is however not possible since a number of the APBs are invisible in the $(220)_S$ lattice fringe image (e.g., the $1/2 [100]$ APB shifts).⁶⁵ However, the APBs where the subdomains are shifted $1/4$ along $[110]$ can be unambiguously characterized by a phase shift of $\pm\pi$ in the phase map of the 220_S lattice fringe image (Figure 6c).⁷⁰ Analysis of the phase maps indicates that the APBs have a thickness of ≈ 1 nm (Figure 6e). Two dislocations in the APB are highlighted by white circles in the lattice fringe image (Figure 6b) and generate discontinuities in the deformation map (Figure 6d). Note that the phase jump indicated by the arrows (from π to $-\pi$, i.e., 2π) does not represent a discontinuity in the phase map and is therefore not a real interface.

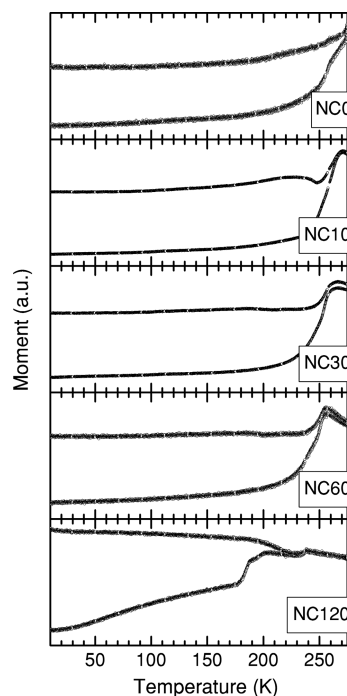


Figure 7. Magnetization vs temperature curves for iron oxide nanocubes NC0–NC120 at different oxidation times. The measurements were carried out using an applied field $H_{\text{app}} = 4$ kA/m (=50 Oe).

TABLE 1. Estimated Blocking Temperatures (T_B) and Corresponding Effective Anisotropy Constant (K_{eff}) of Iron Oxide Nanoparticles at Different Oxidation States

	NC0	NC10	NC30	NC60	NC120
T_B (K)	>275	270	265	255	240
K_{eff} (J/m ³)	$>0.72 \times 10^4$	0.71×10^4	0.69×10^4	0.67×10^4	0.63×10^4

The formation of APBs during the topotaxial transformation of Fe_{1-x}O into $\text{Fe}_{3-\delta}\text{O}_4$ also clarifies the trend of the PXRD diffraction line widths (see Figure 2). The release of microstrain associated with the oxygen fcc sublattice results in the narrowing of the 400_S and the 440_S lines, whereas the 220_S line is only narrowed slightly as a result of the limited growth of the spinel subdomains (separated by APBs). As the particles are oxidized, some of the defects that were initially observed in the nanocrystals (i.e., misfit dislocations) are removed. However, the persistence of the APBs (at 150 °C) is also reflected by the fact that the fwhm of the 220_S diffraction line does not change appreciably, even after extended oxidation times (i.e., for NC240). Previous studies on thin films have concluded that the diffusive motion of the APBs varies considerably with annealing temperature,⁶⁶ thus suggesting that higher temperatures rather than extended times are needed to anneal them out in our IONPs.

The magnetic properties of the IONPs were also studied as a function of their composition during the controlled oxidation of the original core|shell

nanocubes. Temperature-dependent magnetization measurements (shown in Figure 7) were performed on frozen and very dilute (<0.04 vol %) noninteracting nanocube dispersions of NC0–NC120 (see Supporting Information). The approximate values of the blocking temperatures, T_B (*i.e.*, the cusp of the ZFC and FC curves; see Table 1), indicate that the effective anisotropy of nanocubes decreases as the degree of oxidation increases. The core|shell nanocubes NC0 and NC10 display a T_B well above the Néel temperature, T_N , of the Fe_{1-x}O core ($T_N = 198$ K). Although exchange-coupling effects are expected to vanish at T_N , it is not possible to rule out an elevation of T_N as this transition is strongly pressure-dependent ($20\text{ K} \times \text{GPa}^{-1}$ for bulk FeO).⁷¹ Such an effect has previously been observed for the $\text{MnO}|\text{Mn}_3\text{O}_4$ system, where the large pressure exerted by the shell on the core raises the transition temperature relative to that of bulk MnO .⁴⁶ The influence of a strain contribution to the effective anisotropy could also be considered, although theoretical studies suggest that positively strained Fe_3O_4 exhibits a lower magnetocrystalline anisotropy than the unstrained phase.⁷² As the oxidation continues from NC30 to N120, the decrease of T_B can be ascribed to the transformation of magnetite into maghemite with the concomitant lowering of the magnetocrystalline anisotropy. Indeed, using the estimated T_B values and the Néel–Brown equation, it is possible to derive values of the effective anisotropy constant $K_{\text{eff}} = T_B k_B \ln(\tau_m/\tau_0)/V$ (see Table 1), where k_B is the Boltzmann constant, $\tau_0 = 10^{-10}$ s is the inverse attempt frequency,^{73,74} $\tau_m \approx 1$ s is the characteristic measurement time, and $V = 23\text{ nm}^3$ is the volume of a nanocube.

The values obtained for the nanocubes at different degrees of oxidation are close to but below those reported for magnetite.⁷⁵ However, as the oxidation progresses (*i.e.*, for NC10–NC120), the K_{eff} approaches the value reported for $\gamma\text{-Fe}_2\text{O}_3$ ($K_{\text{MC}} = 0.47 \times 10^4\text{ J/m}^3$).⁷³ For small particles (<15 nm), the K_{eff} is strongly influenced by the surface anisotropy, but as the particle size increases, recent studies suggest that the effective anisotropy should converge toward the value of magnetocrystalline anisotropy of the bulk phase.^{15,73} Interestingly, the curve for NC120 shows a fine structure between *ca.* 180 and 250 K, likely arising from the internal defect structure of the nanocubes. Notable is also the suppression of the Verwey transition in all the nanocube samples NC0–NC120, evidenced by the absence of features in the ZFC curves at $T \leq 120$ K. For the oxidized nanocubes NC30–NC120, this is in agreement with previous reports demonstrating a nearly complete suppression of the Verwey transition in oxidized $\text{Fe}_{3-\delta}\text{O}_4$ nanoparticles⁷⁶ and, overall, in particles smaller than 30–40 nm.⁷⁷ For the nanocubes with a stoichiometric or near-stoichiometric composition of the $\text{Fe}_{3-\delta}\text{O}_4$ component (*i.e.*, NC0, NC10), its absence can be attributed to finite size effects and the presence of APBs. Previous work has

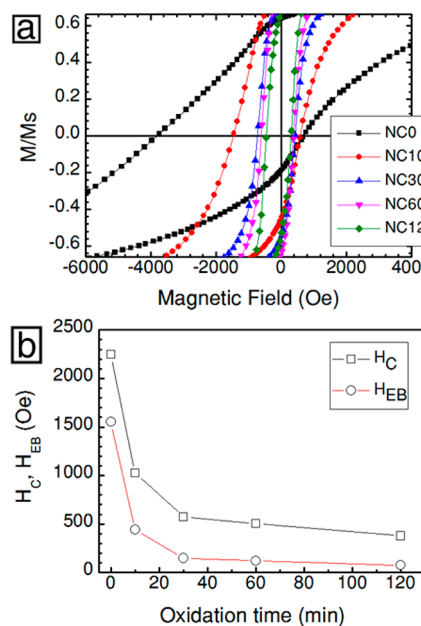


Figure 8. Magnetic measurements of iron oxide nanoparticles at different oxidation times; NC0–NC120. (a) Field-cooled ($H_{\text{FC}} = 4\text{ MA/m} = 50\text{ kOe}$) magnetization vs field hysteresis curves measured at 10 K on dilute dispersions of NC0–NC120 using a maximum field $H_{\text{max}} = 5.6\text{ MA/m} = 70\text{ kOe}$. (b) Variation of exchange bias and coercivity ($H_{\text{EB}}, H_{\text{C}}$) with oxidation time. The lines are a guide for the eye.

demonstrated a complete suppression of the Verwey transition in Fe_3O_4 thin films with a high density of APBs, suggesting that the short-range ordering of cations is inhibiting charge-ordering phenomena.⁷⁸

The saturation magnetization (M_s) and the magnetic particle volume V_{mag} of the as-synthesized core|shell nanocubes (NC0) were determined by measurement of vacuum-dried powder at 305 K. Fitting the high-field part ($\mu_0 H_{\text{max}} > 0.5\text{ MA/m}$) of the magnetization versus field curve to the Langevin equation yields $M_s = 261\text{ kA/m}$ (=50 emu/g) normalized to the inorganic content, and $M_s = 287\text{ kA/m}$ (=55 emu/g) normalized to the $\text{Fe}_{3-\delta}\text{O}_4$ content (see Supporting Information). This is significantly lower than the M_s of bulk Fe_3O_4 (93 emu/g, 290 K)⁷⁹ and $\gamma\text{-Fe}_2\text{O}_3$ (76 emu/g, 293K)⁸⁰ but, interestingly, similar in magnitude as much smaller nanocubes prepared by the same method.^{26,30,81} The magnetic volume $V_{\text{mag}} = 152\text{ nm}^3$ (see Supporting Information) corresponds to a sphere with a diameter of $\approx 6.6\text{ nm}$ (or a cube with an edge length of 5.3 nm) and is considerably smaller than the primary particles and, perhaps not surprisingly, comparable in size to the coherence length determined by the anisotropic Scherrer analysis ($d_{220s} \approx 6.5\text{ nm}$, $d_{400s} \approx 8\text{ nm}$).

Exchange-coupling effects in the oxidized nanocubes were determined from magnetization versus field measurements on very dilute dispersions, in order to avoid the influence of particle interactions. The corresponding hysteresis curves at 10 K are shown in Figure 8a, where it is evident that the shape and

position of the magnetization curves vary considerably with the oxidation state of the particles. For the core|shell cubes (NC0), at $T = 10$ K, we identify a large horizontal displacement of the hysteresis loop, corresponding to an exchange bias $H_{EB} = 1550 \pm 20$ Oe and coercivity of $H_C = 2250 \pm 20$ Oe. The exchange-coupling effects seem to decrease with the oxidation process: for NC10 $H_{EB} = 440 \pm 10$ Oe and $H_C = 1030 \pm 10$ Oe, and for NC30, $H_{EB} = 150 \pm 10$ Oe and $H_C = 550 \pm 10$ Oe. With further oxidization (*i.e.*, NC60, NC120), both H_{EB} and H_C are lowered significantly, but H_{EB} does not vanish (see Figure 8b). The magnitude of H_{EB} and H_C for the NC0 and NC10 nanocubes falls within the range of those reported for $\text{Fe}_{1-x}\text{O}|\text{Fe}_{3-\delta}\text{O}_4$ core|shell systems (*i.e.*, with verified Fe_{1-x}O content); $H_{EB} = 280\text{--}5100$ Oe and $H_C = 540\text{--}4800$ Oe.^{12,13,20\text{--}25,82,83} Note that the relatively large span of reported values seems to originate from large discrepancies in size and composition of the particles.

Classically, exchange bias in nanostructured systems can be characterized by a coupling energy ΔE , which is characteristic for a given FIM|AFM interface.⁸⁴ The areal coupling energy, $\Delta E_A = \Delta E/A = H_{EB}M_s t'_{FIM}$, can be estimated for nanocubes using the FIM/AFM interfacial area per volume term for a core|shell nanocube; $t'_{FIM} = (l_p^3 - l_c^3)/(6l_c^2)$, that is, by using the geometric thickness of the ferrimagnetic component. Here M_s is the saturation magnetization of the FIM component: 287 kA/m (305 K) $\approx 319 \pm 16$ kA/m (10 K),⁵ and l_p and l_c are the edge lengths of the whole nanocube and its core, respectively. In the present case, only NC0, NC10, and possibly NC30 can be considered core|shell systems (see Figures 1–3) and ΔE_A diverges toward unrealistically large values for the single-phase particles NC60 and beyond as l_c becomes negligible. Using the cubic core size determined from PXRD, that is, $l_c = 10.0 \pm 0.5$ and 7.0 ± 1.0 nm for NC0 and NC10 and assuming a value of $l_c = 4.0 \pm 1.0$ nm for NC30 (equivalent to ≈ 0.5 wt % Fe_{1-x}O), we can obtain the geometric thicknesses of the ferromagnetic component for the three cases as $t'_{FIM} = 19 \pm 2$, 39 ± 11 , and 120 ± 40 nm. This corresponds to ΔE_A (10 K): 9.4 ± 1.3 , 5.4 ± 1.6 , and $5.6 \pm 2.9 \times 10^{-4}$ J/m² at 10 K for NC0, NC10, and NC30 respectively. The reduction of ΔE_A regarding NC0 ($l_c = 10$ nm) and NC10 ($l_c = 7$ nm) could be ascribed to the reduction of the Fe_{1-x}O core size. Indeed, a similar effect also occurs in the Co|CoO system where the exchange bias is lowered significantly below a critical CoO thickness.⁸⁵ This is also reflected in previously reported H_{EB} values for $\text{Fe}_{1-x}\text{O}|\text{Fe}_{3-\delta}\text{O}_4$ particles. High values of H_{EB} (> 1500 Oe) have exclusively been reported for larger particles sizes ($l_p > 15$ nm). Smaller particles (10 nm) with comparably small values of t'_{FIM} only exhibit moderate exchange bias effects ($H_{EB} < 500$ Oe).^{12,13,20\text{--}25,82,83}

Interestingly, loop shifts (50–1400 Oe) have also frequently been reported for single-phase Fe_3O_4 and

$\gamma\text{-Fe}_2\text{O}_3$ nanoparticles.^{5,27,28,31–34} Traditionally, such effects have been ascribed to spin-canting or point defects at the particle surface. However, surface effects which are certainly important for smaller particles should scale with the surface to volume ratio and thus diminish drastically as the volume of the particles increases. In a previous study, an exchange bias field of $H_{EB} = 90$ Oe at $T = 10$ K was reported for 12 nm single-phase $\gamma\text{-Fe}_2\text{O}_3$ cubes field-cooled under $H = 10$ kOe.⁸⁶ This is nearly the same value as the exchange bias field of the oxidized single-phase particles (NC120), $H_{EB} = 80 \pm 5$ Oe. The large difference in relative surface area (about 7-fold) between these particles does not agree with a domination of surface effects but suggests that the exchange-coupled components are, instead, located in the bulk of the nanoparticles. Indeed, we have previously observed a reduced saturation magnetization in the nanoparticle cores by polarized SANS measurements.²⁶ The cation disorder at the boundary results in changes of the electronic and magnetic interactions across the APB interface.^{60–62,87} The perturbed cationic ordering modifies the magnetic exchange interactions over the APB. These bring about mostly an antiparallel coupling between the sub-domains across the boundaries.⁶⁵ This results in complicated magnetic structures and reversal processes, which have been the subject of off-axis electron holography and magnetic force microscopy studies.^{69,88} In the system investigated in this study, it is clear that transforming a core|shell IONP by oxidative elimination of the Fe_{1-x}O core generates a material with a finite value of H_{EB} . The nonvanishing exchange bias must be related to the size and order of the $\text{Fe}_{3-\delta}\text{O}_4$ subdomains ($\approx 6\text{--}10$ nm; see Supporting Information, Figure S4) resulting from the order, width, and relative occurrence of APBs. Indeed, a weak exchange bias effect has also been observed in Fe_3O_4 thin films ($H_{EB} = 52$ Oe) and was exclusively linked to the formation of APBs.⁶³ Also, APBs were postulated to be responsible for small H_{EB} in phase pure Fe_3O_4 particles produced by a seeded-growth method.³³ The link between exchange bias and APBs is likely more complex than in conventional exchange-biased systems. In the classical phenomenological model, the polarizable magnetic phase (*i.e.*, the ferrimagnet) is coupled to an AFM phase through an interface. Under the assumption that the anisotropy of the AFM is sufficiently high, the interfacial AFM spins will exert a microscopic torque on the FIM spins. Consequently, a larger field is needed to overcome the torque and to reverse the magnetization, resulting in a loop shift along the field axis.⁸⁹ In contrast to a classical exchange-coupled AFM/FM interfaces, an APB should be considered an interface with a perturbed cationic and magnetic structure rather than a strip of an AFM material. The large high-field susceptibility of single-crystalline Fe_3O_4 materials with a high APB densities⁹⁰ suggests that parts

of the magnetically frustrated interfaces could act as pinning layers. The presence of APBs and other defects in nanoparticles synthesized in organic media also explains why spin-canting effects alone cannot account for the low M_s values observed in single-phase IONPs with a relatively large span of particle sizes.²⁶ This is in agreement with a previous report relating a $\approx 15\%$ reduction of M_s (extrapolated to infinite fields) in Fe_3O_4 thin films, that is, $4.01 \rightarrow 3.45 \mu_B$ to APBs while ruling out the influence of parasitic phases (e.g., $\alpha\text{-Fe}_2\text{O}_3$) and dead interface layers.⁹⁰ Indeed, annealing particles in higher temperatures appears to at least partially recover the M_s of the bulk phase by elimination of APBs. Hai and co-workers treated $\text{Fe}_{3-\delta}\text{O}_4$ nanoparticles in a reducing environment at 260 and 300 °C, thereby increasing the M_s to ≈ 85 emu/g.²² Similarly, in Fe_3O_4 thin films, higher values of M_s could be directly correlated with a decreasing density of APBs.⁹¹ We can therefore conclude that eliminating or at least decreasing the density of APBs is a prerequisite to obtain ferrite nanoparticles with bulk-like properties.

CONCLUSIONS

In summary, we have investigated the complex link between structure and properties in exchange-coupled $\text{Fe}_{1-x}\text{O}|\text{Fe}_{3-\delta}\text{O}_4$ nanocubes synthesized by thermal

decomposition methods during their topotaxial oxidation to single-phase nanocubes. The $\text{Fe}_{1-x}\text{O}|\text{Fe}_{3-\delta}\text{O}_4$ rock salt|spinel interface is the source for a considerable amount of strain, evidenced by lattice parameters deviating significantly from bulk values. The oxidation of the rock salt core toward a spinel structure is reflected by the restricted growth of (strained) ordered spinel subdomain regions and the concomitant relaxation of the oxygen fcc network as the core|shell morphology changes to a single-crystalline state. The formation of APBs during the topotaxial transformation of Fe_{1-x}O (by impinging of the growing spinel subdomains) is the source of a considerable cation disorder in the core|shell particles. These APBs persist during the transformation to single-phase particles, as evidenced by the GPA and PXRD peak width analysis. Magnetic measurements show that, beyond the expected behavior in core|shell nanoparticles, the nonvanishing antiphase boundaries result in a reduced magnetization and exchange bias in single-phase nanoparticles. We can here for the first time link the formation of APBs in the interior of spinel-based nanoparticles with the observed anomalous behavior, whereas the surface effects are negligible. This work also highlights the importance of local structural characterization methods, in addition to bulk methods, that are needed to understand the functional properties of nanomaterials.

EXPERIMENTAL SECTION

Synthesis and Purification of Particles. Iron(III) chloride, (97%, Sigma-Aldrich), sodium oleate, (97%, Tokyo Chemical Industry), oleic acid (99%, Tokyo Chemical Industry), eicosane (99%, Sigma-Aldrich), and cyclooctane (99%, Sigma-Aldrich) were used as received without further purification. Iron(III) oleate was prepared previously as described.^{5,81} In a typical synthesis, 9.5 g of iron(III) oleate (~ 10.25 mmol) and 26.6 g (34 mL) of eicosane were mixed and heated to 60 °C under stirring to melt the eicosane. Oleic acid (1.44 g, 5.12 mmol) and sodium oleate (1.56 g, 5.12 mmol) were added to the solution under constant stirring until the sodium oleate was completely dissolved (≈ 2 h). The mixture was heated to the reflux temperature (≈ 350 °C) in an argon atmosphere under a constant heating rate of $3.3 \text{ }^{\circ}\text{C min}^{-1}$. The solution was left at reflux for 30 min prior to cooling, forming a black waxy solid. To separate the particles, a portion of the waxy solid (≈ 5 g) was dispersed in *n*-heptane (10 mL), and the resulting sol was destabilized by adding ethanol (35 mL). The particles were easily separated from the slurry by centrifugation at 6000 rpm. Repeated washings followed by drying in vacuum yielded a black nanoparticle powder. Thermogravimetric analysis of the vacuum-dried powder was carried out at 800 °C in technical air using a Perkin-Elmer TGA-7, yielding a residue of $\alpha\text{-Fe}_2\text{O}_3$ corresponding to 89 wt % of the original weight. The vacuum-dried nanoparticle powder dispersed poorly in most solvents but was partially dispersible in chlorinated solvents such as CH_2Cl_2 and CHCl_3 .

Postsynthesis Oxidation of Particles. In order to produce a dispersible nanoparticle paste, 105 mg of the vacuum-dried nanoparticle powder was ground in a mortar and soaked in 110 mg of oleic acid and 4 mL of CH_2Cl_2 . The solution was sonicated until the particles were dispersed, after which the CH_2Cl_2 was evaporated. The residual nanoparticle paste was then dispersed in 50 mL of cyclooctane and quickly brought to the reflux temperature (150 °C) in a three-necked round flask.

A stream of dry technical air (20:80 O_2/N_2) was bubbled through the nanoparticle dispersion through a submerged Pasteur pipet (~ 3 bubbles/s). The bubbling of air through the solvent allowed for a controlled solvent reflux while avoiding superheating without the need for mechanical stirring.

Aliquots of the dispersion were extracted after various times of oxidation: 10, 30, 60, 120, 180, and 240 min. The extracted aliquots were stored under an argon atmosphere until they were analyzed. These samples are referred to as NC t , where NC denotes nanocube and t corresponds to the oxidation time. It is important to note that the gentle oxidation method preserves the size and shape of the nanocubes. However, exposure to oxygen and heat results in chemical degradation of the oleic acid surfactant shell,⁹² and the colloidal stability of NC180 and NC240 aliquots was poor. For this reason, they are only used for comparison in the PXRD study.

Powder X-ray Diffraction (PXRD). Cyclooctane dispersions of NC0–NC240 were deposited on Kapton foils and PXRD patterns collected in transmission mode with a Panalytical X'Pert PRO MPD diffractometer ($\lambda(\text{Cu K}\alpha) = 0.15418$ nm), equipped with an X'Celerator detector and a focusing mirror for Cu radiation. Data were collected for $2\theta = 20\text{--}85^\circ$ and a total measuring time of 6 h, using a step size of 0.084° and a setting of the lower PHD setting of 50% to remove fluorescence from Fe, yielding maximum net peak intensities of $\approx 15\,000$ counts. Unit cell parameters and estimations of $\text{Fe}_{1-x}\text{O}|\text{Fe}_{3-\delta}\text{O}_4$ fractions were obtained using the Rietveld method and the FullProf program.⁹³ A preferred Lorentzian size broadening for lines with $h = 2n + 1$ and $k = 2m + 1$ (size model no. 9) was used to improve the fit between observed and calculated patterns. The full width at half-maximum height (fwhm) was for selected lines determined by first stripping the α_2 component and removing the background and then fitting individual lines using the STOE WIN XPOW program and a pseudo-Voigt profile function.

Transmission Electron Microscopy (TEM). The cyclooctane dispersion was diluted in CH_2Cl_2 and evaporated onto ultrathin

carbon-coated grids. HRTEM images and selected area electron diffraction patterns were collected at a JEOL JEM-2100 microscope (LaB₆ filament, 200 kV, $f = 2.7$ mm, $C_s = 1.4$ mm, $C_c = 1.8$ mm, point resolution = 2.5 Å, lattice resolution = 1.4 Å) equipped with a Gatan SC1000 ORIUS camera (for high-resolution imaging) and a Gatan ES500W Erlangshen camera (for diffraction, dark-field imaging) or at a JEOL JEM-2100F microscope (Schottky field-emission gun, 200 kV, $f = 1.9$ mm, $C_s = 0.5$ mm, $C_c = 1.1$ mm, point resolution = 1.9 Å, lattice resolution = 1.0 Å) equipped with a Gatan Ultrascan 1000 camera. Particle size distributions of NCO and NC120 were determined by measuring the edge lengths of 200–300 nanocubes from HRTEM images, and the image magnification was calibrated by comparing the d_{400} or d_{220} lattice spacing with the Fe_{3-x}O₄ lattice parameter determined from PXRD. Geometric phase analysis (GPA)⁵⁵ was used to measure the distortion of lattice fringes with respect to a reference region in a HRTEM image of the particles. We imaged particles close to a ⟨100⟩ zone axis, with the electron dose and acquisition time optimized to avoid beam damage. The measurement and quantitative analysis were performed using the package GPA from HREM Research Inc., a plugin for Gatan Digital Micrograph.

Magnetic Measurements. Magnetic measurements were performed using a Quantum Designs Physical Property measuring system (PPMS-9) equipped with a superconducting magnet and a vibrating sample magnetometer (VSM) option. Magnetic measurements were carried out on (1) vacuum-dried NCO powder at $T = 305$ K and (2) dilute frozen cyclooctane dispersions of NCO–NC120 (<0.04 vol %) at $T = 10$ K using a maximum field $H_{\max} = 1.6$ MA/m (=70 kOe). Agglomerates in the dispersions were allowed to settle prior to sampling of the dispersions. Either a powder sample or 10 µL of the cyclooctane dispersion was transferred into polypropylene sample cups and sealed with epoxy glue. The field-cooled (FC) and zero-field-cooled (ZFC) magnetization measurements were carried out in an applied field $H_{app} = 4$ kA/m (=50 Oe). The exchange bias and coercivity were measured at 10 K by cooling the samples from 270 K under an applied magnetic field $H_{app} \approx 4$ MA/m (=50 kOe).

Conflict of Interest: The authors declare no competing financial interest.

Acknowledgment. This work was financed by Swedish Research Council (VR). The Knut and Alice Wallenberg (KAW) Foundation is acknowledged for providing the electron microscopy facilities and financial support to C.W.T. and G.S.A. under the project 3DEM-NATUR.

Supporting Information Available: Additional characterization: PXRD patterns, electron microscopy images, and magnetic characterization. This material is available free of charge via the Internet at <http://pubs.acs.org>.

REFERENCES AND NOTES

- Colombo, M.; Carregal-Romero, S.; Casula, M. F.; Gutiérrez, L.; Morales, M. P.; Böhm, I. B.; Heverhagen, J. T.; Prosperi, D.; Parak, W. J. Biological Applications of Magnetic Nanoparticles. *Chem. Soc. Rev.* **2012**, *41*, 4306–4334.
- Lee, N.; Hyeon, T. Designed Synthesis of Uniformly Sized Iron Oxide Nanoparticles for Efficient Magnetic Resonance Imaging Contrast Agents. *Chem. Soc. Rev.* **2012**, *41*, 2575–2589.
- Frey, N. A.; Peng, S.; Cheng, K.; Sun, S. Magnetic Nanoparticles: Synthesis, Functionalization, and Applications in Bioimaging and Magnetic Energy Storage. *Chem. Soc. Rev.* **2009**, *38*, 2532–2542.
- Gatteschi, D.; Fittipaldi, M.; Sangregorio, C.; Sorace, L. Exploring the No-Man's Land between Molecular Nanomagnets and Magnetic Nanoparticles. *Angew. Chem., Int. Ed.* **2012**, *51*, 4792–4800.
- Faure, B.; Wetterskog, E.; Gunnarsson, K.; Josten, E.; Hermann, R. P.; Brückel, T.; Andreasen, J. W.; Meneau, F.; Meyer, M.; Lyubartsev, A.; et al. 2D to 3D Crossover of the Magnetic Properties in Ordered Arrays of Iron Oxide Nanocrystals. *Nanoscale* **2013**, *5*, 953–960.
- Yamamoto, K.; Hogg, C. R.; Yamamoto, S.; Hirayama, T.; Majetich, S. A. Dipolar Ferromagnetic Phase Transition in Fe₃O₄ Nanoparticle Arrays Observed by Lorentz Microscopy and Electron Holography. *Appl. Phys. Lett.* **2011**, *98*, 072509.
- Wei, S.; Wang, Q.; Zhu, J.; Sun, L.; Lin, H.; Guo, Z. Multi-functional Composite Core–Shell Nanoparticles. *Nanoscale* **2011**, *3*, 4474–4502.
- Salazar-Alvarez, G.; Lidbaum, H.; López-Ortega, A.; Estrader, M.; Leifer, K.; Sort, J.; Suriñach, S.; Baró, M. D.; Nogués, J. Two-, Three-, and Four-Component Magnetic Multilayer Onion Nanoparticles Based on Iron Oxides and Manganese Oxides. *J. Am. Chem. Soc.* **2011**, *133*, 16738–16741.
- Lee, J.-H.; Jang, J.-T.; Choi, J.-S.; Moon, S. H.; Noh, S.-H.; Kim, J.-W.; Kim, J.-G.; Kim, I.-S.; Park, K. I.; Cheon, J. Exchange-Coupled Magnetic Nanoparticles for Efficient Heat Induction. *Nat. Nanotechnol.* **2011**, *6*, 418–422.
- Park, J.; An, K.; Hwang, Y.; Park, J.-G.; Noh, H.-J.; Kim, J.-Y.; Park, J.-H.; Hwang, N.-M.; Hyeon, T. Ultra-Large-Scale Syntheses of Monodisperse Nanocrystals. *Nat. Mater.* **2004**, *3*, 891–895.
- Shavel, A.; Rodríguez-González, B.; Spasova, M.; Farle, M.; Liz-Marzáñ, L. M. Synthesis and Characterization of Iron/Iron Oxide Core/Shell Nanocubes. *Adv. Funct. Mater.* **2007**, *17*, 3870–3876.
- Hai, H. T.; Yang, H. T.; Kura, H.; Hasegawa, D.; Ogata, Y.; Takahashi, M.; Ogawa, T. Size Control and Characterization of Wüstite (Core)/Spinel (Shell) Nanocubes Obtained by Decomposition of Iron Oleate Complex. *J. Colloid Interface Sci.* **2010**, *346*, 37–42.
- Hai, H. T.; Kura, H.; Takahashi, M.; Ogawa, T. Facile Synthesis of Fe₃O₄ Nanoparticles by Reduction Phase Transformation from γ-Fe₂O₃ Nanoparticles in Organic Solvent. *J. Colloid Interface Sci.* **2010**, *341*, 194–199.
- Hou, Y.; Xu, Z.; Sun, S. Controlled Synthesis and Chemical Conversions of FeO Nanoparticles. *Angew. Chem., Int. Ed.* **2007**, *46*, 6329–6332.
- Demortière, A.; Panissod, P.; Pichon, B. P.; Pourroy, G.; Guillot, D.; Donnio, B.; Bégin-Colin, S. Size-Dependent Properties of Magnetic Iron Oxide Nanocrystals. *Nanoscale* **2011**, *3*, 225–232.
- Bronstein, L. M.; Huang, X.; Retrum, J.; Schmucker, A.; Pink, M.; Stein, B. D.; Dragnea, B. Influence of Iron Oleate Complex Structure on Iron Oxide Nanoparticle Formation. *Chem. Mater.* **2007**, *19*, 3624–3632.
- Redl, F. X.; Black, C. T.; Papaefthymiou, G. C.; Sandstrom, R. L.; Yin, M.; Zeng, H.; Murray, C. B.; O'Brien, S. P. Magnetic, Electronic, and Structural Characterization of Nonstoichiometric Iron Oxides at the Nanoscale. *J. Am. Chem. Soc.* **2004**, *126*, 14583–14599.
- Navrotsky, A.; Mazeina, L.; Majzlan, J. Size-Driven Structural and Thermodynamic Complexity in Iron Oxides. *Science* **2008**, *319*, 1635–1638.
- Bodnarchuk, M. I.; Kovalenko, M. V.; Groiss, H.; Resel, R.; Reissner, M.; Hesser, G.; Lechner, R. T.; Steiner, W.; Schäffler, F.; Heiss, W. Exchange-Coupled Bimagnetic Wüstite/Metal Ferrite Core/Shell Nanocrystals: Size, Shape, and Compositional Control. *Small* **2009**, *5*, 2247–2252.
- Kavich, D.; Dickerson, J.; Mahajan, S.; Hasan, S.; Park, J.-H. Exchange Bias of Singly Inverted FeO/Fe₃O₄ Core–Shell Nanocrystals. *Phys. Rev. B* **2008**, *78*, 174414.
- Sun, X.; Huls, N. F.; Sigdel, A.; Sun, S. Tuning Exchange Bias in Core/Shell FeO/Fe₃O₄ Nanoparticles. *Nano Lett.* **2012**, *12*, 246–251.
- Hai, H. T.; Kura, H.; Takahashi, M.; Ogawa, T. Phase Transformation of FeO/Fe₃O₄ Core/Shell Nanocubes and Facile Synthesis of Fe₃O₄ Nanocubes. *J. Appl. Phys.* **2010**, *107*, 09E301.
- Chen, C.-J.; Chiang, R.-K.; Lai, H.-Y.; Lin, C.-R. Characterization of Monodisperse Wüstite Nanoparticles Following Partial Oxidation. *J. Phys. Chem. C* **2010**, *114*, 4258–4263.
- Pichon, B. P.; Gerber, O.; Lefevre, C.; Florea, I.; Fleutot, S.; Baaziz, W.; Pauly, M.; Ohlmann, M.; Ulhaq, C.; Ersen, O.; et al. Microstructural and Magnetic Investigations of Wüstite-Spinel Core–Shell Cubic-Shaped Nanoparticles. *Chem. Mater.* **2011**, *23*, 2886–2900.

25. Benitez, M. J.; Mishra, D.; Szary, P.; Confalonieri, G. A. B.; Feyen, M.; Lu, A. H.; Agudo, L.; Eggeler, G.; Petracic, O.; Zabel, H. Structural and Magnetic Characterization of Self-Assembled Iron Oxide Nanoparticle Arrays. *J. Phys.: Condens. Matter* **2011**, *23*, 126003.
26. Disch, S.; Wettterskog, E.; Hermann, R. P.; Wiedenmann, A.; Vainio, U.; Salazar-Alvarez, G.; Bergström, L.; Brückel, T. Quantitative Spatial Magnetization Distribution in Iron Oxide Nanocubes and Nanospheres by Polarized Small-Angle Neutron Scattering. *New J. Phys.* **2012**, *14*, 013025.
27. Martinez, B.; Obradors, X.; Balcells, L.; Rouquet, A.; Monty, C. Low Temperature Surface Spin-Glass Transition in γ -Fe₂O₃ Nanoparticles. *Phys. Rev. Lett.* **1998**, *80*, 181–184.
28. Martínez, B.; Roig, A.; Molins, E.; González-Carreño, T.; Serna, C. J. Magnetic Characterization of γ -Fe₂O₃ Nanoparticles Fabricated by Aerosol Pyrolysis. *J. Appl. Phys.* **1998**, *83*, 3256–3262.
29. Goya, G. F.; Berquó, T. S.; Fonseca, F. C.; Morales, M. P. Static and Dynamic Magnetic Properties of Spherical Magnetite Nanoparticles. *J. Appl. Phys.* **2003**, *94*, 3520–3528.
30. Bateer, B.; Tian, C.; Qu, Y.; Du, S.; Tan, T.; Wang, R.; Tian, G.; Fu, H. Facile Synthesis and Shape Control of Fe₃O₄ Nanocrystals with Good Dispersion and Stabilization. *CrystEngComm* **2013**, *15*, 3366–3371.
31. Cannas, C.; Concas, G.; Gatteschi, D.; Falqui, A.; Musinu, A.; Piccaluga, G.; Sangregorio, C.; Spano, G. Superparamagnetic Behaviour of γ -Fe₂O₃ Nanoparticles Dispersed in a Silica Matrix. *Phys. Chem. Chem. Phys.* **2001**, *3*, 832–838.
32. Batlle, X.; Pérez, N.; Guardia, P.; Iglesias, O.; Labarta, A.; Bartolomé, F.; García, L. M.; Bartolomé, J.; Roca, A. G.; Morales, M. P.; et al. Magnetic Nanoparticles with Bulklike Properties (invited). *J. Appl. Phys.* **2011**, *109*, 07B524.
33. Levy, M.; Quarta, A.; Espinosa, A.; Figuerola, A.; Wilhelm, C.; García-Hernández, M.; Genovese, A.; Falqui, A.; Alloyeau, D.; Buonsanti, R.; et al. Correlating Magneto-Structural Properties to Hyperthermia Performance of Highly Monodisperse Iron Oxide Nanoparticles Prepared by a Seeded-Growth Route. *Chem. Mater.* **2011**, *23*, 4170–4180.
34. Guardia, P.; Labarta, A.; Batlle, X. Tuning the Size, the Shape, and the Magnetic Properties of Iron Oxide Nanoparticles. *J. Phys. Chem. C* **2011**, *115*, 390–396.
35. Morales, M. P.; Serna, C. J.; Bødker, F.; Mørup, S. Spin Canting Due to Structural Disorder in Maghemite. *J. Phys.: Condens. Matter* **1997**, *9*, 5461–5467.
36. Kodama, R.; Berkowitz, A. Atomic-Scale Magnetic Modeling of Oxide Nanoparticles. *Phys. Rev. B* **1999**, *59*, 6321–6336.
37. Kodama, R.; Berkowitz, A.; McNiff, E., Jr.; Foner, S. Surface Spin Disorder in NiFe₂O₄ Nanoparticles. *Phys. Rev. Lett.* **1996**, *77*, 394–397.
38. Curiale, J.; Granada, M.; Troiani, H. E.; Sánchez, R. D.; Leyva, A. G.; Levy, P.; Samwer, K. Magnetic Dead Layer in Ferromagnetic Manganite Nanoparticles. *Appl. Phys. Lett.* **2009**, *95*, 043106.
39. Dey, P.; Nath, T. K.; Banerjee, A. Enhanced Grain Surface Effect on Magnetic Properties of La_{0.5}Gd_{0.2}Sr_{0.3}MnO₃ Nanoparticles: A Comparison with Bulk Counterpart. *Appl. Phys. Lett.* **2007**, *91*, 012504.
40. Kodama, R. Magnetic Nanoparticles. *J. Magn. Magn. Mater.* **1999**, *200*, 359–372.
41. Luijjes, B.; Woudenberg, S. M. C.; de Groot, R.; Meeldijk, J. D.; Torres Galvis, H. M.; de Jong, K. P.; Philipse, A. P.; Erné, B. H. Diverging Geometric and Magnetic Size Distributions of Iron Oxide Nanocrystals. *J. Phys. Chem. C* **2011**, *115*, 14598–14605.
42. McCammon, C. A.; Liu, L. The Effects of Pressure and Temperature on Nonstoichiometric Wüstite, Fe_xO: The Iron-Rich Phase Boundary. *Phys. Chem. Miner.* **1984**, *10*, 106–113.
43. Salazar-Alvarez, G.; Sort, J.; Suriñach, S.; Baró, M. D.; Nogués, J. Synthesis and Size-Dependent Exchange Bias in Inverted Core–Shell MnO|Mn₃O₄ Nanoparticles. *J. Am. Chem. Soc.* **2007**, *129*, 9102–9108.
44. López-Ortega, A.; Tobía, D.; Winkler, E.; Golosovsky, I. V.; Salazar-Alvarez, G.; Estradé, S.; Estrader, M.; Sort, J.; González, M. A.; Suriñach, S.; et al. Size-Dependent Passivation Shell and Magnetic Properties in Antiferromagnetic/Ferrimagnetic Core/Shell MnO Nanoparticles. *J. Am. Chem. Soc.* **2010**, *132*, 9398–9407.
45. Golosovsky, I.; Salazar-Alvarez, G.; López-Ortega, A.; González, M.; Sort, J.; Estrader, M.; Suriñach, S.; Baró, M.; Nogués, J. Magnetic Proximity Effect Features in Antiferromagnetic/Ferrimagnetic Core–Shell Nanoparticles. *Phys. Rev. Lett.* **2009**, *102*, 247201.
46. Silva, N. J. O.; Kharmaoui, M.; Amaral, V. S.; Puente-Orench, I.; Campo, J.; da Silva, I.; Ibarra, A.; Bustamante, R.; Millán, A.; Palacio, F. Shell Pressure on the Core of MnO/Mn₃O₄ Core/Shell Nanoparticles. *Phys. Rev. B* **2013**, *87*, 224429.
47. Will, G.; Hinze, E.; Nuding, W. The Compressibility of FeO Measured by Energy Dispersive X-ray Diffraction in a Diamond Anvil Squeezer up to 200 kbar. *Phys. Chem. Miner.* **1980**, *167*, 157–167.
48. Cornell, R.; Schwertmann, U. *The Iron Oxides: Structure, Properties, Reactions, Occurrences and Uses*, 2nd ed.; John Wiley & Sons, Ltd.: New York, 2003; p 175.
49. Koga, K.; Zubia, D. Strain Analysis of Au_xCu_{1-x}Cu₂O Biphase Nanoparticles with Heteroepitaxial Interface. *J. Phys. Chem. C* **2008**, *112*, 2079–2085.
50. Mittemeijer, E. J.; Welzel, U. The “State of the Art” of the Diffraction Analysis of Crystallite Size and Lattice Strain. *Z. Kristallogr.* **2008**, *223*, 552–560.
51. Li, Z. Characterization of Different Shaped Nanocrystallites Using X-ray Diffraction Line Profiles. *Part. Part. Syst. Charact.* **2012**, *28*, 19–24.
52. Larsson, M. W.; Wagner, J. B.; Wallin, M.; Håkansson, P.; Fröberg, L. E.; Samuelson, L.; Wallenberg, L. R. Strain Mapping in Free-Standing Heterostructured Wurtzite InAs/InP Nanowires. *Nanotechnology* **2007**, *18*, 015504.
53. Hytch, M. J.; Houdellier, F. Mapping Stress and Strain in Nanostructures by High-Resolution Transmission Electron Microscopy. *Microelectron. Eng.* **2007**, *84*, 460–463.
54. Taraci, J. L.; Hytch, M. J.; Clement, T.; McCartney, M. R.; Drucker, J.; Picraux, S. T. Strain Mapping in Nanowires. *Nanotechnology* **2005**, *16*, 2365–2371.
55. Hytch, M. J.; Snoeck, E.; Kilaas, R. Quantitative Measurement of Displacement and Strain Fields from HREM Micrographs. *Ultramicroscopy* **1998**, *74*, 131–146.
56. Rouvière, J. L.; Sarigiannidou, E. Theoretical Discussions on the Geometrical Phase Analysis. *Ultramicroscopy* **2005**, *106*, 1–17.
57. Ding, Y.; Sun, X.; Wang, Z. L.; Sun, S. Misfit Dislocations in Multimetallic Core-Shelled Nanoparticles. *Appl. Phys. Lett.* **2012**, *100*, 111603.
58. Hazen, R. M.; Jeanloz, R. Wüstite (Fe_{1-x}O): A Review of Its Defect Structure and Physical Properties. *Rev. Geophys.* **1984**, *22*, 37–46.
59. Backhaus-Ricoult, M.; Dieckmann, R. Defects and Cation Diffusion in Magnetite (VII): Diffusion Controlled Formation of Magnetite during Reactions in the Iron–Oxygen System. *Ber. Bunsen Ges. Phys. Chem.* **1986**, *90*, 690–698.
60. Voogt, F.; Palstra, T.; Niesen, L.; Rogojanu, O.; James, M.; Hibma, T. Superparamagnetic Behavior of Structural Domains in Epitaxial Ultrathin Magnetite Films. *Phys. Rev. B* **1998**, *57*, R8107–R8110.
61. Rudee, M. Antiphase Domain Boundaries in Thin Films of Magnetite. *Microsc. Microanal.* **1997**, *126*–129.
62. Margulies, D.; Parker, F.; Rudee, M.; Spada, F.; Chapman, J.; Aitchison, P.; Berkowitz, A. Origin of the Anomalous Magnetic Behavior in Single Crystal Fe₃O₄ Films. *Phys. Rev. Lett.* **1997**, *79*, 5162–5165.
63. Arora, S. K.; Sofin, R. G. S.; Nolan, A.; Shvets, I. V. Antiphase Boundaries Induced Exchange Coupling in Epitaxial Fe₃O₄ Thin Films. *J. Magn. Magn. Mater.* **2005**, *286*, 463–467.
64. Bobo, J. F.; Basso, D.; Snoeck, E.; Gatel, C.; Hrabovsky, D.; Gauffier, J. L.; Ressier, L.; Mamý, R.; Visnovsky, S.; Hamrlé, J.; et al. Magnetic Behavior and Role of the Antiphase Boundaries in Fe₃O₄ Epitaxial Films Sputtered on MgO (001). *Eur. Phys. J. B* **2001**, *24*, 43–49.
65. Celotto, S.; Eerenstein, W.; Hibma, T. Characterization of Anti-phase Boundaries in Epitaxial Magnetite Films. *Eur. Phys. J. B* **2003**, *36*, 271–279.

66. Eerenstein, W.; Palstra, T.; Hibma, T.; Celotto, S. Diffusive Motion of Antiphase Domain Boundaries in Fe_3O_4 Films. *Phys. Rev. B* **2003**, *68*, 014428.
67. Hibma, T.; Voogt, F. C.; Niesen, L.; van der Heijden, P. A. A.; de Jonge, W. J. M.; Donkers, J. J. T. M.; van der Zaag, P. J. Anti-phase Domains and Magnetism in Epitaxial Magneteite Layers. *J. Appl. Phys.* **1999**, *85*, 5291–5293.
68. Parkinson, G.; Manz, T.; Novotný, Z.; Sprunger, P.; Kurtz, R.; Schmid, M.; Sholl, D.; Diebold, U. Antiphase Domain Boundaries at the $\text{Fe}_3\text{O}_4(001)$ Surface. *Phys. Rev. B* **2012**, *85*, 195450.
69. Kasama, T.; Dunin-Borkowski, R.; Eerenstein, W. Off-Axis Electron Holography Observation of Magnetic Microstructure in a Magnetite (001) Thin Film Containing Antiphase Domains. *Phys. Rev. B* **2006**, *73*, 104432.
70. Tai, C. W.; Lereah, Y. Quantitative Strain-Field Measurement of 1:1 B-Site Cation Ordered Domains and Antiphase Boundaries in $\text{Pb}(\text{Sc}_{1/2}\text{Ta}_{1/2})\text{O}_3$ Ceramics by High-Resolution Transmission Electron Microscopy. *Appl. Phys. Lett.* **2009**, *94*, 051908.
71. Kantor, I.; Dubrovinsky, L.; Mccammon, C.; Dubrovinskia, N.; Goncharenko, I.; Kantor, A.; Kuznetsov, A.; Crichton, W. FeO and MnO High-Pressure Phase Diagrams: Relations between Structural and Magnetic Properties. *Phase Transiti.* **2007**, *80*, 1151–1163.
72. Jeng, H.-T.; Guo, G. First-Principles Investigations of the Electronic Structure and Magnetocrystalline Anisotropy in Strained Magnetite Fe_3O_4 . *Phys. Rev. B* **2002**, *65*, 094429.
73. Rebbouh, L.; Hermann, R.; Grandjean, F.; Hyeon, T.; An, K.; Amato, A.; Long, G. Fe⁵⁷ Mössbauer Spectral and Muon Spin Relaxation Study of the Magnetodynamics of Monodispersed $\gamma\text{-Fe}_2\text{O}_3$ Nanoparticles. *Phys. Rev. B* **2007**, *76*, 174422.
74. Bedanta, S.; Kleemann, W. Supermagnetism. *J. Phys. D: Appl. Phys.* **2009**, *42*, 013001.
75. Cullity, B. D.; Graham, C. D. *Introduction to Magnetic Materials*, 2nd ed.; John Wiley & Sons: New York, 2009; p 383.
76. Takai, S.; Atake, T.; Koga, Y. Heat Capacity Anomalies at the Verwey Transition of $\text{Fe}_{3(1-\delta)}\text{O}_4$. *Thermochim. Acta* **1994**, *246*, 1–10.
77. Özdemir, Ö.; Dunlop, D. J.; Moskowitz, B. M. The Effect of Oxidation on the Verwey Transition in Magnetite. *Geophys. Res. Lett.* **1993**, *20*, 1671–1674.
78. Eerenstein, W.; Palstra, T.; Hibma, T.; Celotto, S. Origin of the Increased Resistivity in Epitaxial Fe_3O_4 Films. *Phys. Rev. B* **2002**, *66*, 201101.
79. O'Handley, R. C. *Modern Magnetic Materials: Principles and Applications*; John Wiley & Sons: New York, 2000; p 740.
80. Berkowitz, A. E. Influence of Crystallite Size on the Magnetic Properties of Acicular $\gamma\text{-Fe}_2\text{O}_3$ Particles. *J. Appl. Phys.* **1968**, *39*, 1261–1263.
81. Disch, S.; Wetterskog, E.; Hermann, R. P.; Salazar-Alvarez, G.; Busch, P.; Brückel, T.; Bergström, L.; Kamali, S. Shape Induced Symmetry in Self-Assembled Mesocrystals of Iron Oxide Nanocubes. *Nano Lett.* **2011**, *11*, 1651–1656.
82. Chalasani, R.; Vasudevan, S. Form, Content, and Magnetism in Iron Oxide Nanocrystals. *J. Phys. Chem. C* **2011**, *115*, 18088–18093.
83. Sharma, S. K.; Vargas, J. M.; Pirotta, K. R.; Kumar, S.; Lee, C. G.; Knobel, M. Synthesis and Ageing Effect in FeO Nanoparticles: Transformation to Core–Shell FeO/ Fe_3O_4 and Their Magnetic Characterization. *J. Alloys Compd.* **2011**, *509*, 6414–6417.
84. Nogués, J.; Sort, J.; Langlais, V.; Skumryev, V.; Suriñach, S.; Muñoz, J. S.; Baró, M. D. Exchange Bias in Nanostructures. *Phys. Rep.* **2005**, *422*, 65–117.
85. Nogués, J.; Skumryev, V.; Sort, J.; Stoyanov, S.; Givord, D. Shell-Driven Magnetic Stability in Core–Shell Nanoparticles. *Phys. Rev. Lett.* **2006**, *97*, 157203.
86. Salazar-Alvarez, G.; Qin, J.; Sepelák, V.; Bergmann, I.; Vasilakaki, M.; Trohidou, K. N.; Ardisson, J. D.; Macedo, W. A. A.; Mikhaylova, M.; Muhammed, M.; et al. Cubic versus Spherical Magnetic Nanoparticles: The Role of Surface Anisotropy. *J. Am. Chem. Soc.* **2008**, *130*, 13234–13239.
87. Brabers, V. Ferrimagnetic Insulators. In *Handbook of Magnetism and Advanced Magnetic Materials*; John Wiley & Sons, Ltd.: New York, 2007.
88. Pan, Q.; Pokhil, T. G.; Moskowitz, B. M. Domain Structures in Epitaxial (110) Fe_3O_4 Particles Studied by Magnetic Force Microscopy. *J. Appl. Phys.* **2002**, *91*, 5945–5950.
89. Nogués, J.; Schuller, I. K. Exchange Bias. *J. Magn. Magn. Mater.* **1999**, *192*, 203–232.
90. Moussy, J.-B.; Gota, S.; Bataille, A.; Guittet, M.-J.; Gautier-Soyer, M.; Delille, F.; Dieny, B.; Ott, F.; Doan, T.; Warin, P.; et al. Thickness Dependence of Anomalous Magnetic Behavior in Epitaxial $\text{Fe}_3\text{O}_4(111)$ Thin Films: Effect of Density of Antiphase Boundaries. *Phys. Rev. B* **2004**, *70*, 174448.
91. Magen, C.; Snoeck, E.; Lüders, U.; Bobo, J. F. Effect of Metallic Buffer Layers on the Antiphase Boundary Density of Epitaxial Fe_3O_4 . *J. Appl. Phys.* **2008**, *104*, 013913.
92. Roonasi, P.; Holmgren, A. A Fourier Transform Infrared (FTIR) and Thermogravimetric Analysis (TGA) Study of Oleate Adsorbed on Magnetite Nano-particle Surface. *Appl. Surf. Sci.* **2009**, *255*, 5891–5895.
93. Rodríguez-Carvajal, J. Recent Advances in Magnetic Structure Determination by Neutron Powder Diffraction. *Physica B* **1993**, *192*, 55–69.